Geochemistry Geophysics Geosystems G3

Article
Volume 14, Number 8
28 August 2013
doi: 10.1002/ggge.20213
ISSN: 1525-2027

Published by AGU and the Geochemical Society

Electrical conductivity of the Pampean shallow subduction region of Argentina near 33 S: Evidence for a slab window

Aurora I. Burd and John R. Booker
Department of Earth and Space Sciences, University of Washington, Box 351310, Seattle, Washington, 98195, USA (aburd@uw.edu)

Randall Mackie
Land General Geophysics, CGG, Milan, Italy

Cristina Pomposiello and Alicia Favetto
Instituto de Geocronología y Geología Isotopíca, Universidad de Buenos Aires, CONICET, Buenos Aires, Argentina

[1] We present a three-dimensional (3-D) interpretation of 117 long period (20–4096 s) magnetotelluric (MT) sites between 31°S and 35°S in western Argentina. They cover the most horizontal part of the Pampean shallow angle subduction of the Nazca Plate and extend south into the more steeply dipping region. Sixty-two 3-D inversions using various smoothing parameters and data misfit goals were done with a nonlinear conjugate gradient (NLCG) algorithm. A dominant feature of the mantle structure east of the horizontal slab is a conductive plume rising from near the top of the mantle transition zone at 410 km to the probable base of the lithosphere at 100 km depth. The subducted slab is known to descend to 190 km just west of the plume, but the Wadati-Benioff zone cannot be traced deeper. If the slab is extrapolated downdip it slices through the plume at 250 km depth. Removal of portions of the plume or blocking vertical current flow at 250 km depth significantly changes the predicted responses. This argues that the plume is not an artifact and that it is continuous. The simplest explanation is that there is a "wedge"-shaped slab window that has torn laterally and opens down to the east with its apex at the plume location. Stress within the slab and seismic tomography support this shape. Its northern edge likely explains why there is no deep seismicity south of 29°S.

Components: 17,802 words, 12 figures, 2 tables.

Keywords: three-dimensional magnetotelluric inversion; slab window; Nazca flat slab subduction.

Index Terms: 1515 Geomagnetic induction: Geomagnetism and Paleomagnetism; 8104 Continental margins: convergent: Tectonophysics; 8170 Subduction zone processes: Tectonophysics; 8413 Subduction zone processes: Volcanology; 7270 Tomography: Seismology; 9360 South America: Geographic Location.

Received 19 March 2013; **Revised** 21 June 2013; **Accepted** 24 June 2013; **Published** 28 August 2013.

Burd, A. I., J. R. Booker, R. Mackie, M. C. Pomposiello, and A. Favetto (2013), Electrical conductivity of the Pampean shallow subduction region of Argentina near 33 S: Evidence for a slab window, *Geochem. Geophys. Geosyst.*, *14*, 3192–3209, doi:10.1002/ggge.20213.

© 2013. American Geophysical Union. All Rights Reserved.

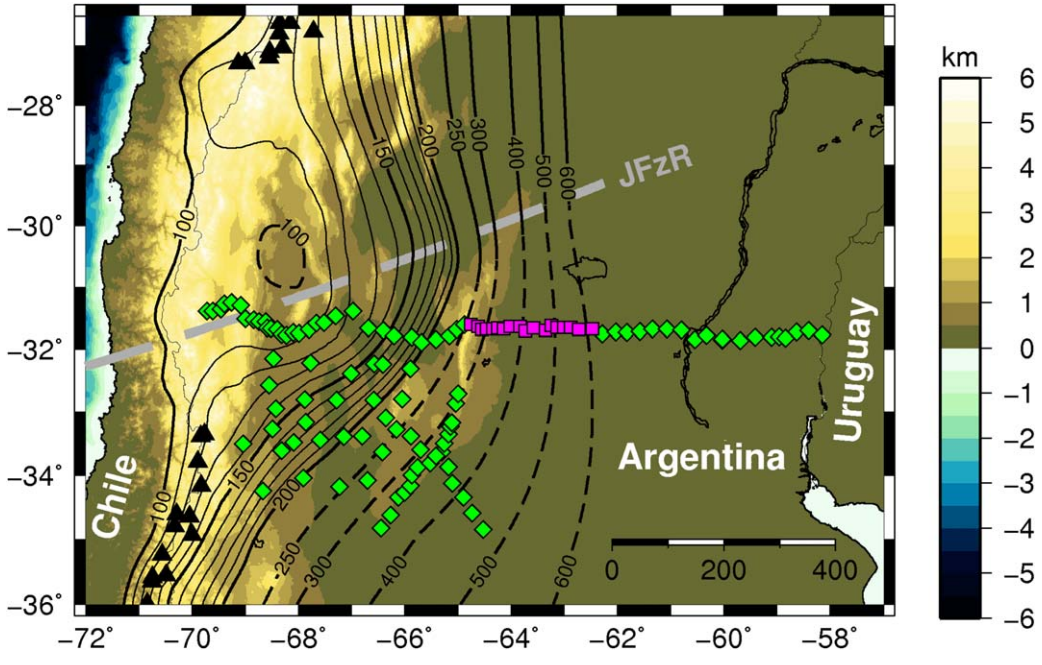

Figure 1. MT Site locations on a topographic map of South America, with slab contours from Appendix A. The green diamonds are MT sites, magenta squares are MT sites used in both this paper and *Booker et al*. [2004], black triangles are geologically young Southern and Central Volcanic Zone volcanoes, and the dashed gray line is the subducted Juan Fernandez Ridge (JFzR).

1. Introduction

[2] The subducted Nazca slab beneath Chile and western Argentina, near 31.5°S, levels out at about 100 km depth and then dips more steeply into the mantle several hundred kilometers to the east [*Cahill and Isacks*, 1992; *Anderson et al*., 2007; *Linkimer Abarca*, 2011] (see Figure 1). While deep earthquakes north of 29°S locate the slab to a depth exceeding 600 km, the Pampean shallow subduction region does not appear to have any Wadati-Benioff zone earthquakes deeper than 195 km [*International Seismological Centre, EHB Bulletin*, 2010]. The flat slab prevents formation of an asthenospheric wedge under the Andes and consequently there are no active volcanoes. South of 33.3°S in the Andean Southern Volcanic Zone (SVZ), the slab steepens to 36° [*Cahill and Isacks*, 1992; *Pesicek et al*., 2012], an asthenospheric wedge forms and there are active volcanoes. The prevailing view is that the Nazca slab is warped continuously between its flat and dipping segments. For a concise review of Pampean shallow subduction, see *Ramos* [2009].

[3] The resistive crust of the Pampean region permits long period magnetotelluric data to image conductivity at depths of 300 km or more [*Booker et al*., 2004], and suggests the slab dips steeply at the same longitude as the deep earthquakes north of 29°S. However, the robust result of *Booker et al*. [2004] is that there is vertical current flow at this location and hence a vertical conductor (see Figure 2). Identification of this conductor with the slab location rests only on its coincidence with southward extrapolation of the very deep earthquakes and the suggestion that the vertical current path is a consequence of penetration of the slab into the transition zone. Thus, the location (or even the existence) of the flat Nazca slab after it descends below 200 km is uncertain.

2. Methods

[4] The magnetotelluric (MT) method uses passively recorded electric and magnetic field data at Earth's surface to probe electrical conductivity below Earth's surface. Electrical conductivity (with units of Siemens per meter) is strongly sensitive to changes in phase (which depends on temperature and pressure), water content, and melt fraction, but between roughly 100 and 400 km depth, elevated conductivity of the upper mantle is more likely the result of partial melt or other interconnected fluids than hydrous minerals [*Yoshino et al*., 2009]. Because conductivity at upper mantle

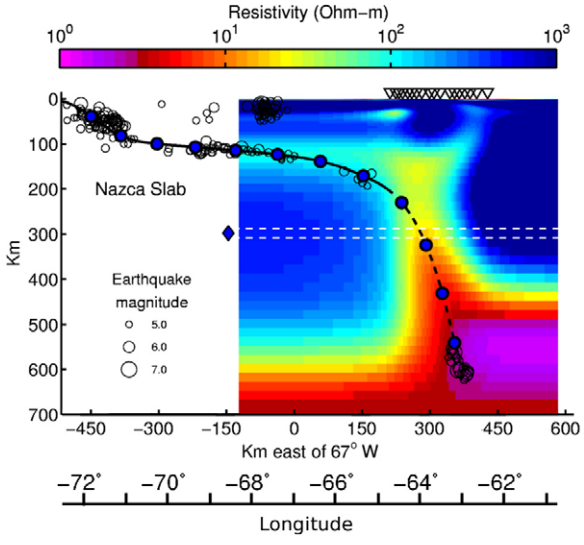

Figure 2. Two-dimensional electrical resistivity model from *Booker et al*. [2004]. Triangles are MT sites (see Figure 1). The depth of the subducted Nazca slab shallower than 200 km is based on the earthquake hypocenters (open circles) between 30°S and 32°S projected on the transect at 31.4°S. The slab deeper than 200 km is shown dashed because it is a smooth interpolation using hypocenters deeper than 500 km, from between 29°S and 28°S, projected south to the transect. Circles filled with blue along the Nazca slab are at intervals of 1 Ma since subduction. The layer delineated by dashed lines and flagged by the filled diamond was used by *Booker et al*. [2004] to show that vertical current flow is required at that depth. This conclusion remains valid for our 3-D study, but the 3-D structure deeper than 200 km differs significantly, because the main locus of vertical current flow is not directly beneath the 2-D profile. Thus, the remarkable coincidence of the extrapolated deep earthquakes with the base of the conductive feature that rises upward to 100 km is an artifact of the 2-D model assumption.

conditions is $<<1$, it is usual to use its reciprocal, resistivity (with units of Ohm m).

[5] From 2000 to 2009, we collected more than 200 MT sites across Argentina, of which 117 between latitudes 29°S and 35°S were used for this study (see Figure 1). Analysis of 37 additional sites south of 35°S is in A. I. Burd et al., Three-dimensional electrical conductivity in the mantle beneath the Payún Matrú Volcanic Field in the Andean back-arc of Argentina near 36.5° S: Decapitation of a mantle plume by resurgent upper mantle shear during slab steepening?, submitted to *Geophysics Journal International*, 2013. Each site consists of 5 to 15 days of horizontal electric field (**E**, with units of mV/km) and three-component magnetic field (**H**, with units of nT) time series sampled at 0.25 s with Narod Intelligent Magnetotelluric Systems (NIMS) or at 5 s with Long-period Intelligent Magnetotelluric Systems (LIMS). The nominally 100 m long electric field dipoles used Pb-$PbCl_2$ electrodes [*Petiau*, 2000].

[6] Time series data were processed using the robust multi-station algorithm of *Egbert* [1997] to determine the MT impedance tensor **Z** and the vertical to horizontal magnetic field transfer function **W**, which is also known as the induction vector. These complex frequency-domain transfer functions between the components of the electric and magnetic fields can be written:

$$\begin{bmatrix} E_x \\ E_y \end{bmatrix} = \begin{bmatrix} Z_{xx} & Z_{xy} \\ Z_{yx} & Z_{yy} \end{bmatrix} \begin{bmatrix} H_x \\ H_y \end{bmatrix} \quad (1)$$

$$[H_z] = [W_x \quad W_y] \begin{bmatrix} H_x \\ H_y \end{bmatrix} \quad (2)$$

[7] Each of the elements of **Z** and **W** in equations (1) and (2) has a real and imaginary part, or equivalently, a phase and magnitude. For the impedance tensor, the phases of the impedance elements are defined as

$$\phi_{ij} = tan^{-1}\left(\frac{Im(Z_{ij})}{Re(Z_{ij})}\right) \quad (3)$$

and the magnitudes are commonly converted to apparent resistivities

$$\rho_{a,ij} = 0.2T|Z_{ij}|^2 \quad (4)$$

where T is the period in seconds. The units of ρ_a are Ohm m when the units of Z_{ij} are *mV/km/nT*. All data were processed identically so that they are directly comparable. These data are available through the IRIS Data Management System, Seattle, Washington.

[8] A major step forward in MT interpretation was the realization that Z can be distorted by unresolvable small-scale structure. When this distortion is due to electric charge that is in phase with the larger scale "regional" electric field, it is termed static or Galvanic and is a common problem. When the distortion is frequency independent and the regional (large-scale) structure is two-dimensional (2-D) it is possible to extract an estimate of the undistorted regional impedance using techniques that have come to be called "impedance tensor decomposition" [*Bahr*, 1988; *Groom and Bailey*, 1989; *Jones*, 2012]. However, when the regional structure is not strictly 2-D, tensor

decomposition becomes an invalid statistical model because it cannot fit noise-free measured data [*Caldwell et al.*, 2004; *Booker*, 2013].

[9] To avoid this fundamental issue, *Caldwell et al.* [2004] introduced the impedance "phase tensor"

$$\mathbf{\Phi} = (Re(\mathbf{Z}))^{-1} Im(\mathbf{Z}) = \begin{bmatrix} \Phi_{xx} & \Phi_{xy} \\ \Phi_{yx} & \Phi_{yy} \end{bmatrix} \quad (5)$$

$$= \mathbf{R}^{-1}(\theta) \begin{bmatrix} \Phi_a & 0 \\ 0 & \Phi_b \end{bmatrix} \mathbf{R}(\psi)\mathbf{R}(\theta) \quad (6)$$

which is unaffected by static distortion and makes no assumptions about the dimensionality of the regional structure. The parameterization (6) is related to the geometry of the "phase tensor ellipse" that results when $\mathbf{\Phi}$ multiplies the unit circle [*Caldwell et al.*, 2004; *Booker*, 2013]. $\mathbf{R}$ is the unitary matrix that rotates Cartesian coordinates through an angle, θ is the direction of one of the axes of the ellipse, $|\Phi_a|$ and $|\Phi_b|$ are the lengths of the ellipse semiaxes and

$$\psi = \tan^{-1}\left(\frac{\Phi_{xy} - \Phi_{yx}}{\Phi_{xx} + \Phi_{yy}}\right) \quad (7)$$

is the "normalized phase tensor skew angle." ψ is rotationally invariant and can be computed in any coordinate system. (Note that ψ is twice the skew angle β defined by *Caldwell et al.* [2004]).

[10] If the structure is 2-D, ψ must be zero and the principle phases $\phi_a = tan^{-1}(\Phi_a)$ and $\phi_b = tan^{-1}(\Phi_b)$ equal the phases of the off-diagonal elements of $\mathbf{Z}$ in the coordinate system aligned with the ellipse axes (i.e., the strike). In that coordinate system the diagonal elements of the 2-D regional $\mathbf{Z}$ are 0. If ψ is not zero, the regional structure must be 3-D. If $|\psi| = 6^\circ$, the magnitudes of the diagonal elements of regional $\mathbf{Z}$ in ellipse-aligned coordinates are 10% of the off-diagonal elements [*Booker*, 2013]. Thus, $|\psi| > 6^\circ$ is a good working criterion for concluding that the data must be 3-D. $|\psi| < 6^\circ$ can be considered "quasi-2-D," but may still be 3-D.

[11] *Booker et al.* [2004] analyzed a subset of eighteen of our sites shown as magenta squares in Figure 1. They used a 2-D nonlinear conjugate gradient (NLCG) minimum structure inversion [*Rodi and Mackie*, 2001]. However, Figure 3 also shows ψ at all periods at our 117 sites. Data that meet the quasi-2-D criterion of $|\psi| < 6^\circ$ are colored green. It is quite obvious that the data are significantly 3-D at most sites and all periods and that deviation from 2-D behavior is quite large, particularly at longer periods, along the profile used by *Booker et al.* [2004].

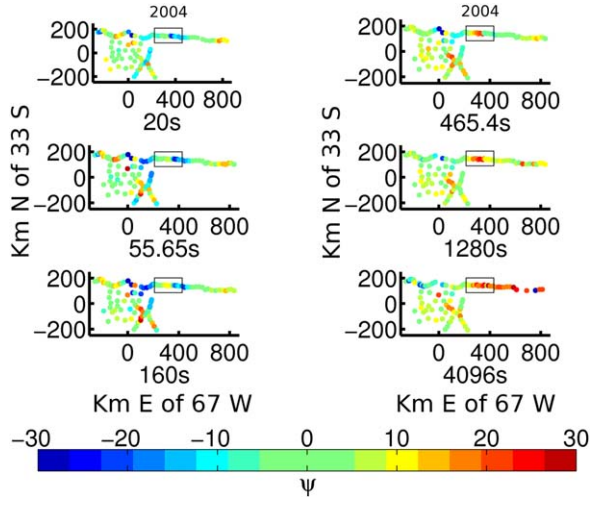

Figure 3. Plots of normalized phase tensor skew angle, ψ, for most sites, at each period used in the inversion (some of the Eastern-most sites have been cropped from these images). $|\psi| < 6$ is compatible with 2-D interpretation (shown in green in this figure), so most sites are clearly significantly 3-D. Small boxes labeled 2004 are sites used in *Booker et al.* [2004].

[12] $\mathbf{Z}$ and $\mathbf{W}$ have six complex elements. Their real and imaginary parts constitute twelve responses, which are sensitive to different aspects of resistivity structure. We directly invert the real and imaginary parts of Z_{xx}, Z_{yy}, W_x, and W_y. However, instead of directly inverting the real and imaginary parts of the off-diagonal elements Z_{xy} and Z_{yx}, we use their phases and the natural logs of their magnitudes. All twelve inverted responses are in the coordinate system with x = true north and y = true east.

[13] We invert the data using a 3-D NLCG minimum structure algorithm (based on *Mackie et al.* [2001]), which seeks a model that minimizes an objective function,

$$S = \chi^2 + \tau R(m) \quad (8)$$

where τ is a trade-off parameter, $R(m)$ is a measure of model "roughness" and

$$\chi^2 = \sum_{i=1}^{N} \frac{r_i^2}{\sigma_i^2} \quad (9)$$

is a measure of data misfit. The r_i^2 are the square of the data residuals (e.g., predicted values–observed values), σ_i^2 are the variances, and N is the number

of data. The trade-off parameter τ was adjusted between inversion runs in order to minimize S while keeping χ^2 and $\tau R(m)$ of similar order of magnitude so that neither is overly important. This results in the model that is smoothest (i.e., has least complicated structure) for a given misfit. More complicated models may fit the data equally well but their additional features are not required.

[14] Our algorithm uses weighted least squares. Data with statistically derived error estimates σ_i smaller than a threshold called the "error floor" are weighted equally while data with larger error estimates are down weighted. This weighting scheme is implemented by increasing estimated uncertainties below the error floor up to the floor. Henceforth, the σ_i refer to data errors after the error floors have been applied.

[15] Instead of χ^2 it is common to give the "normalized root-mean-square"(nRMS),

$$nRMS = \sqrt{\frac{\chi^2}{N}} \tag{10}$$

as the misfit measure because it would be 1.0 if each datum had a misfit equal to its estimated error.

[16] Roughness $R(m)$ can be defined as the square of the Laplacian of the model, averaged over the model. However, because spatial resolution decreases with depth due to the diffusive physics of MT, we modify this definition so that the structure penalty in all spatial directions increases with depth. Making x, y, and z increase logarithmically rather than linearly with depth, a three-dimensional version of the argument of *Smith and Booker* [1991] shows that

$$R(\mathbf{m}) = \int_{model} \left[f_x \frac{\partial^2 \mathbf{m}}{\partial x^2} + f_y \frac{\partial^2 \mathbf{m}}{\partial y^2} + \frac{\partial^2 \mathbf{m}}{\partial z^2} \right]^2 (z + z_0) dx dy dz \tag{11}$$

[17] The small-scale z_0 prevents the structure penalty from becoming zero at Earth's surface. The weighting functions

$$f_x = MAX\left(1.0, \frac{\Delta x_i}{\Delta z_k}\right) \tag{12}$$

$$f_y = MAX\left(1.0, \frac{\Delta y_i}{\Delta z_k}\right) \tag{13}$$

compensate for variable horizontal block widths near the surface, where Δx_i and Δy_i are horizontal block widths in the model and Δz_k is the thickness of each block. $\Delta x_i/\Delta z_k$ and $\Delta y_i/\Delta z_k$ are the block aspect ratios. The weighting functions also account for the large aspect ratios of near-surface blocks that lead to high horizontal roughness.

[18] All models terminate in a 3 Ohm m half-space deeper than 660 km. A deep resistivity of this order is widely accepted based on mantle conditions and minerals [*Xu et al*., 2000]. In some of our inversions, a "tear" is added at 410 km depth, at which the smoothing is not enforced in any direction. This discontinuity allows assessment of the degree to which this bottom half space has been smoothed upward into the rest of the model, as well as whether the data are sensitive to structure below the depth of the tear.

[19] Furthermore, *Xu et al*. [1998] find that at the top of the mantle transition zone (MTZ), which extends from 410 to 660 km, upper mantle olivine changes phase to MTZ minerals such as wadsleyite and ringwoodite that are at least an order of magnitude less resistive. *Yoshino* [2010] also documents a decrease in resistivity of at least an order of magnitude at 410 km. Thus there is a geophysical reason to permit a discontinuous change in resistivity at 410 km.

[20] The inversions include electrically conductive oceans. The importance of the Pacific Ocean in 2-D inversions of our data was shown by *Booker et al*. [2005] and the importance of both Pacific and Atlantic Oceans in 3-D is discussed by A. I. Burd and J. R. Booker (manuscript in preparation, 2013). In order to keep the mesh size relatively small while accurately modeling the effect of ocean bathymetry, we used an ocean of constant depth but varying electrical conductance. (Conductance [Siemens] = layer thickness [m] ÷ electrical resistivity [Ohm m].) This layer has high resistivity when the water is shallow, and low resistivity when the water is deep. The ocean layers and the discontinuity between land and water are excluded from the $R(m)$ computation, and the ocean depth and resistivity are held fixed.

3. Results

[21] Sixty-two inversions were done using a range of periods, misfit goals, error thresholds, and structure penalty parameters. In order to compare models computed in different ways against each other, forward calculations were made for all models using the same $R(m)$, the same six periods from 20

Table 1. Selected Inversion Results[a]

Inversion Name	a53	a58	a62
Global nRMS	1.91	2.08	2.32
Roughness	5.7×10^6	4.0×10^6	1.3×10^6
Number of iterations	252	152	170

[a]See text for discussion of each quantity.

to 4096 s, and the same error thresholds: 2% for $|Z_{xy}|$ and $|Z_{yx}|$ (equivalent to 1.2° for ϕ_{xy} and ϕ_{yx} and 4% for the apparent resistivities). The error thresholds for the real and imaginary parts of Z_{xx} are equal to the absolute error threshold of $|Z_{xy}|$, similarly for Z_{yy} and $|Z_{yx}|$.

[22] The nRMS and roughness values computed in this way are compared for three inversions in Table 1. Each of these inversions was iterated until the objective function (8) could no longer be reduced and is considered fully converged. Based on its nRMS, "a53" has the best fit to the observed data but is rougher, while "a58" is not as tightly fit and is smoother. Model "a62" has a "tear" at 410 km (as mentioned above in the "Methods" section). Its roughness can not be directly compared to a53 and a58, due to the tear.

[23] Model a53 is considered better because its nRMS is smallest and all its major features are present in the less tightly fitting and smoother models a58 and a62. While the global nRMS shown in Table 1 is useful for comparing different inversions, Figure 4 shows the nRMS at each site and period used in a53. We should expect $nRMS \sim 1.0$ at every site and period. Values less than 0.75 represent fitting the data too tightly (i.e., overfit), while those greater than 1.25 can be considered under-fit. Values of nRMS between 0.75 and 1.25 are ideal and are shown in green. Since most sites are green at periods longer than 56 s, the global nRMS of 1.91 is largely due to larger misfits at the shortest periods. This is likely the result of trying to fit the responses of shallow structure that have spatial scales smaller than the site spacing and means that the shallow structure is less reliable than deeper structure.

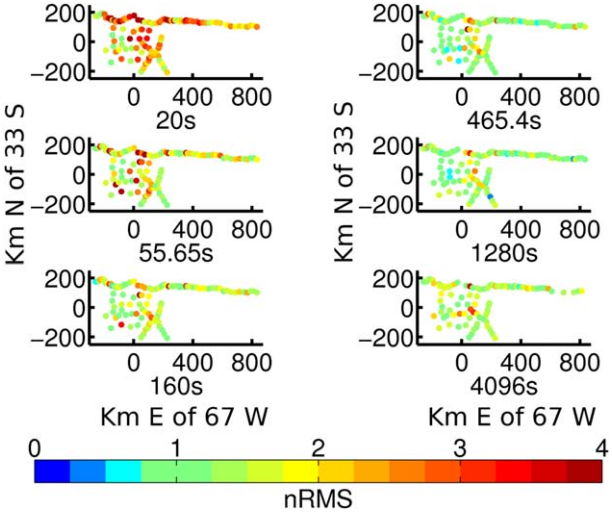

Figure 4. Maps showing nRMS at each site at each period for a53. Site locations are indicated by the colored circles, where the color corresponds to the nRMS at that site. Note that $0.75 < nRMS < 1.25$ are green to indicate sites at which the inversion was able to adequately fit the data. See text for discussion of why the misfit is not as good at the shorter periods.

[24] Figure 5a shows east-west oriented vertical slices through a53. The feature we are concentrating on in this paper is the prominent southwesterly dipping conductive plume-like structure between 100 and 410 km depth in the east half of slice *C* (structure indicated as "plume" in Figure 5a). Note that it is deeper and more westerly in slice *B* and shallower and more easterly in slice *D*. The plume's core is over 2 orders of magnitude more conductive than the surrounding mantle. This feature is evident in much smoother models that have higher nRMS values and changes little in models that have tears at 410 km (including a62, which is shown in Figure 6).

[25] Appendix A discusses estimation of the subducted slab surface. Figure 5a shows that the extrapolation of the slab intersects the conductive core of the plume at about 250 km depth. Figure 5b shows the map view of the slab contours from Figure 1 with 10 Ohm m contours of the model added at 200 km, 250 km, and 350 km depths: the slab and plume intersect at 250 km. Figure 5c shows the 10 Ohm m isosurface of the model in red with the subducting slab in shades of green indicating depth, where it is obvious that slab and plume intersect.

[26] It is common at this point in seismological tomographic studies to use "checkerboard" tests in which data computed for a model of alternating blocks are inverted to investigate the resolution of the inversions. However, the different physics of MT makes such tests misleading at best and therefore of little use.

[27] Body wave tomography uses travel time along rays. The ability to resolve a structure depends on the density and angular dispersion of the rays in and adjacent to each block of the checkerboard

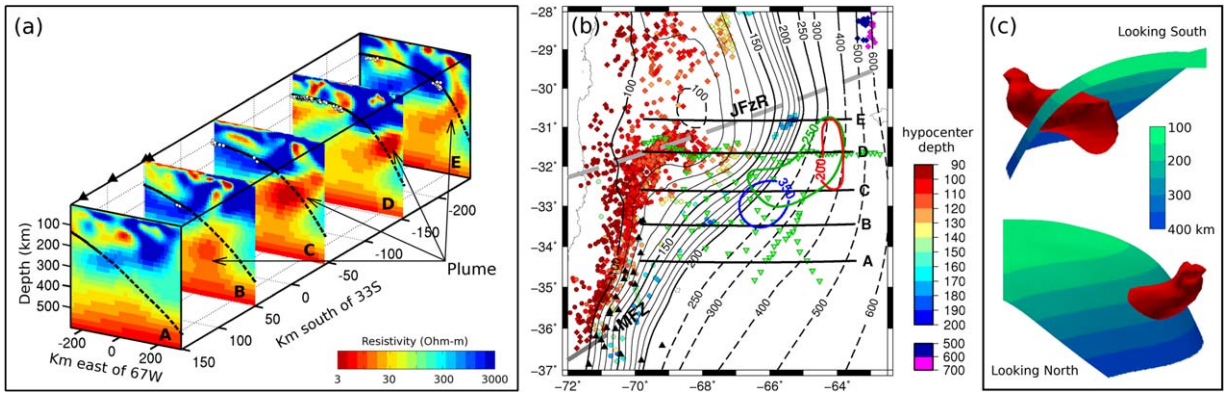

Figure 5. (a) East-West slices of resistivity for inversion a53. Black triangles are Southern Volcanic Zone volcanoes, black lines and dashed lines are location of subducted Nazca slab, based on the slab surface discussed in Appendix A. White points are earthquakes. Scale is stretched North-South to improve viewing. The origin (0,0) = 67° W, 33° S. (b) Position of slices in Figure 5a are shown as solid black lines. Green triangles are MT sites, dashed gray line is the subducted Juan Fernandez Ridge (JFzR), gray line is the subducted Mocha Fracture Zone (MFZ). Black triangles are volcanoes. See Appendix A for discussion of earthquakes and slab contours. 10 Ohm m contours of the conductive plume are shown at 200, 250, and 350 km depth. Earthquakes are color-coded by depth. Note that the 200 km plume contour overlaps the location of the 2-D plume identified in *Booker et al*. [2004] (Figure 2). (c) 10 Ohm m isosurface in red with surface representing subducting slab in shades of green: (top) the view to the South (including the underside of the subducting slab), (bottom) the view to the North.

and there is no fundamental difference between 2-D and 3-D.

[28] MT resolution depends on: (1) whether electromagnetic energy can penetrate through the host to the target; (2) how much current is induced in the target; and (3) the geometry of the target. Energy penetration decreases in a given material as induced current goes up. Thus, shallow conductive blocks in a checkerboard shield energy from reaching deeper blocks precisely when deeper blocks are ideal for significant induction of current. Consequently, a deep block with a resistive overburden may be well resolved when a checkerboard test concludes it cannot be.

[29] One role of target geometry arises because induced currents must close on themselves. In a conductive cube at depth, current flows in circles within the cube. The radiated secondary field of a deep cube that must be sensed at Earth's surface in order to detect the cube falls off as the inverse cube of distance even without consideration of the skin depth in the host. On the other hand, strike-aligned currents induced in a 2-D checkerboard model are line currents that close at infinity. Their radiated fields fall off only as the inverse of distance. Thus MT resolution depends strongly on the aspect ratio of the target. Consequently, elongated structures may be well resolved when a checkerboard test with equant blocks concludes it cannot be.

[30] Finally, the general 3-D situation for MT is even more complicated. For instance, when two conductive layers are connected by a small vertical conductive prism through the intervening resistive layer and at least one of the conductive layers has some horizontal variation, current induced in the conductive layers will flow through the vertical connection and "light it up." The same is true for

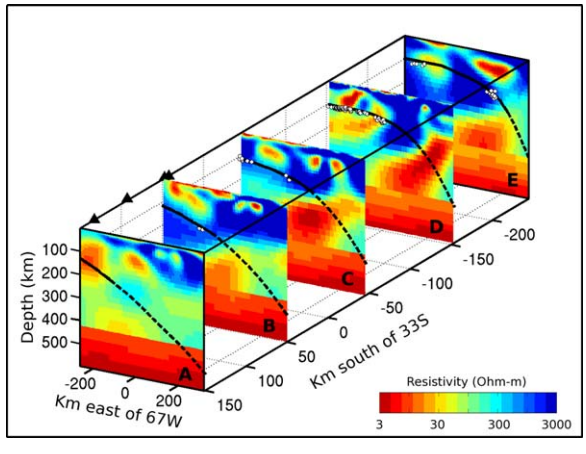

Figure 6. East-West slices of resistivity for inversion a62. Slice positions are shown in Figure 5b. Black triangles are Southern Volcanic Zone volcanoes, black lines and dashed lines are location of subducted Nazca slab, based on the slab surface discussed in Appendix A. White points are earthquakes. Scale is stretched North-South to improve viewing. The origin (0,0) = 67° W, 33° S.

horizonal connections between larger scale conductive regions. This very important behavior is responsible for the MT signature of the conductive plume in this 3-D study. It cannot be addressed by a checkerboard.

[31] No general answer to the MT resolution issue has yet been formulated. We thus performed hypothesis tests to answer several questions:

[32] 1. Is the inversion unduly influenced by the bottom boundary condition of a 3 Ohm m halfspace at 700 km?

[33] 2. Is the conductive plume an artifact of the inversion?

[34] 3. Is the conductive plume present above the subducted slab's predicted intersection with the plume location near 250 km depth?

[35] 4. Is the conductive plume present below the subducted slab's predicted intersection with the plume?

[36] 5. Is the conductive plume continuous through the predicted intersection with the slab at 250 km?

[37] 6. Is the conductive plume continuous through 350 km depth and thus probably connected to the mantle transition below 410 km?

[38] With the exception of interpretation of the effects of the tear in model a62, we used the following procedure to conduct these tests: to determine whether a structure in a particular model is significant, we remove it from the model and see if the responses change by substantially more than the data error. Removing a structure from a converged minimum-structure model is a definitive test of whether the structure is required for the given inversion parameters. In this context, we use the data errors after the error floors have been applied because this presents a more challenging test for significance.

[39] For all test results excluding a62's tear, we present two characteristic ratios calculated at each site and period used in the inversion. The first is the ratio of nRMS of the test model to its unperturbed value nRMS_0. For brevity, we write

$$P = \frac{nRMS}{nRMS_0} \tag{14}$$

[40] The second is the absolute change in normalized phase tensor skew angle relative to its estimated error, which we write:

$$\delta\psi_\sigma = \frac{|\psi - \psi_0|}{\sigma} = \frac{|\Delta\psi|}{\sigma} \tag{15}$$

where σ is the estimated error of ψ with error floors applied.

[41] P is useful because it includes both impedance tensor and vertical field data. If all data had the same errors, the error would cancel out of P and P would not depend on the error. In practice, however, data do not all have the same errors, but in our inversion, the error floors make the data errors similar in size and thus P depends only weakly on estimated error and choice of error floor. $\delta\psi_\sigma$ is useful because it is unaffected by shallow distortion, combines all elements of the impedance tensor and is sensitive to changes in structural dimensionality.

[42] When $P = 1$ there has been no change in nRMS, when $P < 1$ the nRMS has decreased (unlikely, but still a possibility), and when $P > 1$ the nRMS has increased. When $P > 2$, it means that the misfit of every datum has on average doubled, which represents very significant worsening of the fit. When $\delta\psi_\sigma < 1$ then $\Delta\psi$ is insignificant relative to its error, when $1 < \delta\psi_\sigma < 2$ then $\Delta\psi$ is moderately in excess of its error, and when $\delta\psi_\sigma > 2$ then $\Delta\psi$ is at least twice the size of its error.

[43] Values of both ratios less than one are plotted in green on Figures 7 and 8 because these values mean that the structural change is allowed by the data. Then we cannot assign geological importance to the structure being tested. On the other hand, $P > 1$ at many sites or $P > 2$ at a few sites can be considered large enough that the change in structure strongly affects the data. In that case, we can be confident that the original structure is not an artifact. Since $\delta\psi_\sigma$ is primarily related to the change in dimensionality of the model and Tests 2 to 6 only change structure near the plume, we expect $\delta\psi_\sigma$ to be much more localized than P. Thus $\delta\psi_\sigma > 1$ at several sites or $\delta\psi_\sigma > 2$ at a few sites indicate that the change in dimensionality of the structure is significant.

[44] We removed conductive structures using a "thresholding" scheme, in which all values with resistivity below 100 Ohm m were replaced by the largest nearby value. This allows the structure to cease to exist, while avoiding creation of new contrasting structure. In a few cases, however, where we wished to suppress all current flow through a particular structure, we replaced a portion of the conductive structure with very high resistivity

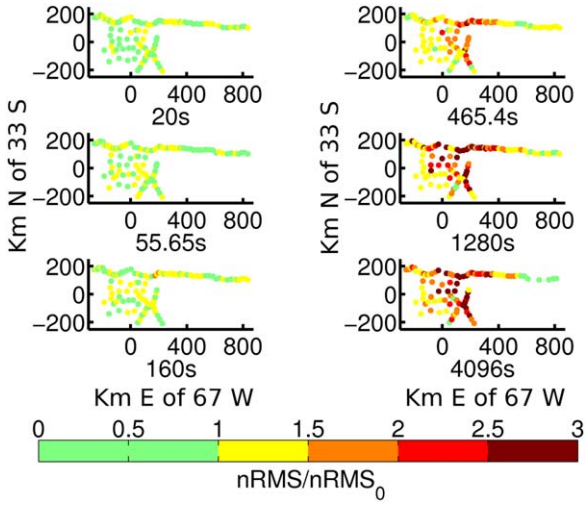

Figure 7. Map views showing $P = nRMS/nRMS_0$ at each site in the main part of the array at each period with the conductive plume removed (Test 2 as discussed in the text). Green values are considered insignificant change from the original model. Note that the effect of removing the plume is larger at periods of 465.4 s or longer. This affects the 465.4 s data because the overlying crust is so resistive.

(10,000 Ohm m) instead of the more "neutral" structure created using the thresholding scheme. We never use a resistive layer across the entire model because to do so would suppress all vertical current flow, which in particular would significantly alter the effects of the oceans. In general, these structural changes make the test models less 3-D. Table 2 compiles the results of Tests 2–6 at 1280 s, including the global nRMS found after each test and the number of sites where $1 < P < 2$, $P > 2$, $1 < \delta\psi_\sigma < 2$, and $\delta\psi_\sigma > 2$. 1280 s exhibits the strongest effects. We also present global nRMS using all sites and periods for each test, but we do not compute a global P, since sites far from the test structure and periods insensitive to the test structure will typically cause P to always be close to 1.

3.1. Test 1: Sensitivity to Structure Below 410 km

[45] Figure 6 shows the results of inversion a62, which has a "tear" at 410 km depth. If the data were not sensitive to structure below the depth of the tear, the region below the tear would have resistivity values identical to the bottom boundary condition of 3 Ohm m because that is the smoothest possible structure below the tear. Structure below 410 km is visible in all slices, so the data are sensitive to structure below the depth of the tear. In addition, structure above the depth of the tear appears very similar to structure in a53. We conclude that upward smoothing of the fixed

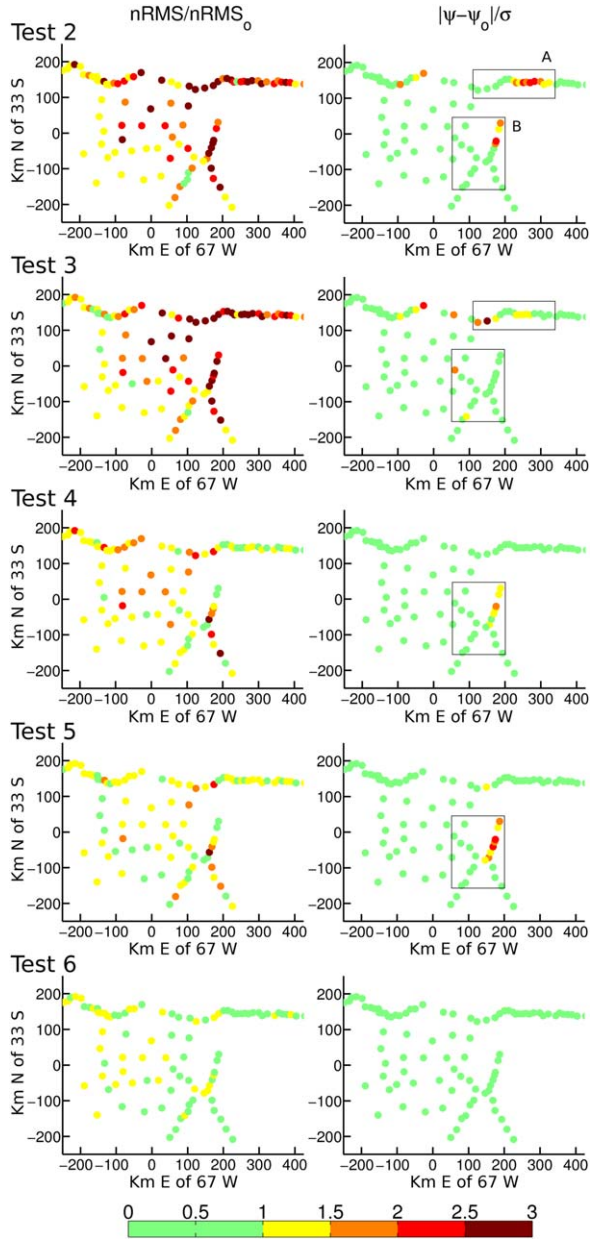

Figure 8. Maps of ratios P and $\delta\psi_\sigma$ at 1280 s period at each site for structural hypothesis tests, displaying only sites in the main array near the conductive plume: (Test 2) conductive plume removed; (Test 3) conductive plume removed above 250 km depth; (Test 4) conductive plume removed below 250 km depth; (Test 5) conductive plume replaced with 10,000 Ohm m layer at 250 km depth; and (Test 6) conductive plume replaced with 10,000 Ohm m layer at 350 km depth. In all images, green dots mean that the model change is allowed by the data; red implies that the model change is forbidden by the data. Boxes A and B are only shown in the figure and discussed in the text where $\delta\psi_\sigma > 1$.

Table 2. Hypothesis Test Results at 1280 s[a]

Test	Global nRMS	$1 < P < 2$	$P > 2$	$1 < \delta\psi_\sigma < 2$	$\delta\psi_\sigma > 2$
2	2.39	66	40	13	4
3	2.52	60	40	12	2
4	2.06	71	8	6	0
5	1.99	72	2	7	2
6	1.92	43	0	0	0

[a]A total of 114 sites were used at this period for the P tests and 111 for the $\delta\psi_\sigma$-tests: columns other than Global nRMS indicate the number of sites in each category. See text for discussion of each test. Global nRMS represents nRMS at all sites and periods used in the inversion.

bottom boundary has little effect on the model above 410 km.

3.2. Test 2: Existence of Overall Plume

[46] Figure 7 shows P at all periods when the conductive plume is removed, and Figure 8 (Test 2) shows P and $\delta\psi_\sigma$ at 1280 s. Responses longer than 400 s have $P > 2$ at many sites, indicating that the conductive plume is not an artifact of the inversion. Sites with $\delta\psi_\sigma > 1$ are primarily located in two regions: box A in Figure 8 (Test 2) along the main east-west profile and box B, slightly to the south-west. These regions correspond to the location of the plume. Table 2 shows that all four P and $\delta\psi_\sigma$ criteria for the structure not being an artifact are met. This test confirms the presence of the conductive feature but does not determine whether it is a single feature or multiple features smeared together.

3.3. Test 3: Existence of Plume Above Expected Slab Location

[47] Figure 8 (Test 3) shows P and $\delta\psi_\sigma$ for 1280 s when the upper portion of the plume is removed. Compared to removing the entire plume in Test 2, the visual impression of the P map is not quite as strong but there are still many sites with $P > 2$. Sites where $\delta\psi_\sigma > 1$ are mainly located in box A. This is exactly what we expect because this box is above the shallow part of the plume. Table 2 shows that all four P and $\delta\psi_\sigma$ criteria are met, indicating that the portion of the plume above 250 km depth is indeed required by the data.

3.4. Test 4: Existence of Plume Below Slab Location

[48] Figure 8 (Test 4) shows P and $\delta\psi_\sigma$ when the lower portion of the plume is removed. The visual impression of the P map is more subdued than Test 3 but the perturbation in P are still clearly significant. The only sites with $\delta\psi_\sigma > 1$ are in box B which Figure 5b shows is above the part of the slab deeper than 250 km, as expected. Table 2 shows that three of the four P and $\delta\psi_\sigma$ criteria are met, so we conclude that the portion of the plume below 250 km depth is also required by the data.

3.5. Test 5: Continuity of Plume Through Predicted Slab Intersection

[49] To test whether electric current flows vertically through the extrapolated slab location, we introduce a horizontal highly resistive 500 km $\times$ 500 km thin layer extending across the plume region at 250 km depth. This suppresses all vertical current flow through 250 km at the plume location, and is similar to a test used by *Booker et al.* [2004] to conclude that 2-D vertical flow of current from below 200 km is required.

[50] Figure 8 (Test 5) shows the P and $\delta\psi_\sigma$ at 1280 s. The P test results are similar in magnitude to Test 4, although somewhat differently arrayed spatially. Like Test 4, the only sites with $\delta\psi_\sigma > 1$ are in box B but show a larger effect. Table 2 shows that all four of the P and $\delta\psi_\sigma$ criteria are met. We therefore conclude that vertical current flow is required by the data, and that there is a single-plume extending through the estimated slab location at 250 km depth.

3.6. Test 6: Vertical Current Flow Between Plume and Transition Zone

[51] Figure 5a shows the plume emerging from the top of a widespread deep conductor that extends across the entire model, which can reasonably be identified with a conductive mantle transition zone that begins at 410 km, but the deepest layer at which the plume is readily identifiable as a conductive zone in a resistive environment is slightly shallower, at 350 km. Thus we introduce a horizontal highly resistive 500 km $\times$ 750 km layer at 350 km to block vertical current flow between the plume and the transition zone.

[52] Figure 8 (Test 6) shows that no sites have $P > 2$ or $\delta\psi_\sigma > 1$ at 1280 s; however, 40 sites spread over much of the main array have $P > 1$. Table 2 shows that only one of the P criteria and none of the $\delta\psi_\sigma$ criteria are met. Tables 1 and 2 also show that the global nRMS of this test is nearly the same as the global nRMS of a53, which suggests that most values of P are actually near 1. Based on our criteria, we can not conclude that vertical current flow through 350 km is required by the data. However, Test 6 may be inadequate because the

model at this depth is in general more conductive, so it is harder to block the three-dimensional flow of current with a resistive layer local to the plume. Therefore current may easily flow around the resistive layer, causing P and $\delta\psi_\sigma$ to be near 1 at most sites, yielding a misleading conclusion.

4. Discussion

[53] Our tests show that the conductive plume is required by the data, and the data require the plume to be a continuous feature above 350 km, which passes through the estimated slab location. Similar tests were performed on model a62, with identical outcomes.

[54] There are at least three possible scenarios that allow electric current to flow through the estimated slab location: (1) the slab is sufficiently deformed so that the plume is always east of the slab; (2) there is a window in the slab where the plume and slab intersect; and (3) a deep plume impinges on the slab and generates a shallow plume that is electrically but not mechanically connected to the deep plume.

[55] The first possibility seems untenable. Figure 5b shows that the 10 Ohm m contour passes under the 170 km slab contour at 31.5°S. This contour is constrained by hypocenters within a degree to the southwest and northwest and within half a degree updip. Thus a continuous slab that remains west of the plume would need to fold back on itself and dip steeply westward between 32 and 33°S. However the tomographic model of *Pesicek et al.* [2012] images the slab at 35°S with an average eastward dip of 36° from 200 to 400 km depth while the deep seismicity at 29°S implies an eastward slab dip of about 65° (see Appendix A). Consequently, a reverse dip between 32 and 33°S would require an unlikely amount of distortion.

[56] The second alternative is supported by three lines of evidence: observed stress within the slab, seismic tomography and our electrical conductivity structure. Intermediate depth subduction zone earthquakes are expected to exhibit downdip tension and normal faulting when the subducted slab is mechanically continuous to deeper depths, because the denser, deeper slab pulls on the buoyant, shallower slab. Regional studies of slab stress in the Chile-Argentina subduction zone [*Chen et al.*, 2001; *Slancová et al.*, 2000; *Anderson et al.*, 2007; *Pardo et al.*, 2002] support this concept. However, *Anderson et al.* [2007] find focal mechanism tension (T) axes for events about 120 km deep within the box labeled A in Figure 9 to be predominantly along the depth contours (i.e., perpendicular to their expected direction) and they suggest a slab window roughly coincident with the aseismic dashed ovoid to the east-southeast of their box.

[57] Figure 9 also shows four focal mechanism beachballs for the best double-couple Centroid Moment Tensors (http://www.globalcmt.org/CMTsearch.html, Global Centroid Moment Tensor solutions) deeper than 150 km and northeast of box A. Their T, P (compression) and nodal axes are shown on a stereo plot in the inset. Although their P and nodal axes directions are diverse, their T axes are closely grouped with a mean direction to the northeast and a dip near 20°. Like the *Anderson et al.* [2007] events, this direction is not perpendicular to the subducting slab's contours, but instead points toward the southern end of the very deep seismicity at 29°S. This suggests that while the slab may be continuous between these four events and the deep events, the subducted slab is missing to the south-east.

[58] Figure 10 shows horizontal and vertical slices of the global seismic tomography model of *Li et al.* [2008]. These slices show the percentage change of compressional body wave velocity V_p with respect to the assumed radially symmetric background. The horizontal block dimensions are $0.7^\circ \times 0.7^\circ$ and the vertical thicknesses are 45.2 km. Although one needs to be cautious about local inferences from global seismic tomography, there is a remarkable coincidence between features of this model and our conductive plume. The horizontal slice on the left is centered at 249 km depth. North of 31°S it has high velocity that compares very well with the 250 km estimated slab contour. South of 31°S this slab signature essentially terminates and appears to resume again to the southwest. The 10 Ohm m contour of the conductive plume at 250 km depth fits neatly into the gap in the slab signature. The vertical slice of δV_p at slice D of Figure 5 is shown on the right of Figure 10. Again there is high velocity that can be associated with the Nazca Slab shallower than 200 km and deeper than 350 km. Between 200 and 350 km the slab signature is missing. The 10 and 30 Ohm m contours of the conductive plume fit neatly into this gap. These correspondences seem unlikely to be fortuitous and we conclude that the slab is missing where it would intersect the plume. Deeper than 350 km, the high seismic velocity suggests that the slab is present again. However, the slab

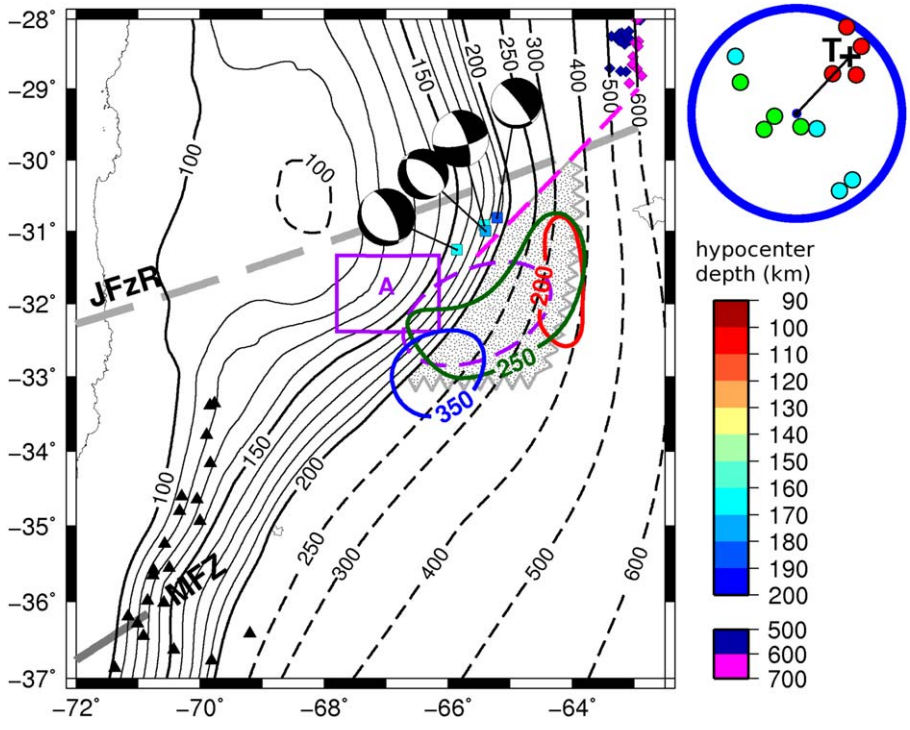

Figure 9. Focal mechanism beachballs for four Global Centroid Moment Tensors [http://www.globalcmt.org/CMTsearch.html]. Tensional (red), compressional (green), and nodal (cyan) axes for these events are shown in the inset. JFzR = Juan Fernandez Ridge, MFZ = Mocha Fracture Zone. 10 Ohm m plume contours are shown at 200, 250, and 350 km depth. *Anderson et al*. [2007] identify a region of contour-parallel tensional axes in purple box labeled "A" and suggest the possibility of a slab gap in the aseismic region within the purple dashed ovoid. Southern Volcanic Zone volcanoes = black triangles. Stippled gray area is the minimum size of slab window necessary to pass the conductive plume. Serration of the east and south edges indicates that the window may actually extend much further in these directions.

signature arguably dips westward below this depth and in the deep MTZ and top of the lower mantle below 660 km ends up beneath the apparent source of the conductive plume. This suggests that the deeper slab signature may not be the Nazca Slab, but a relic of earlier, westward dipping subduction. In fact, *Pesicek et al*. [2012] use regional seismic tomography to suggest a relic slab slightly to the west of the modern Nazca slab south of 38°S.

[59] The gray stippled area in Figure 9 shows the approximate minimum extent of the slab window necessary to allow the plume to pass through. The western boundary is the 200 km slab contour, as the slab is relatively well located to this depth. The northern boundary is parallel to the T axes of the four earthquakes discussed earlier in this section, and its eastward extension passes through the southern termination of the very deep seismicity. It is shown with a dashed line because its exact position is uncertain. The eastern boundary is based on the deep slab δV_p signature seen in Figure 10. However, it is possible that the slab window continues downward to the east, as this would explain why there are no very deep earthquakes south of 29°S; this is also compatible with our results, so the eastern boundary is shown as a serrated edge. The southern extent of the slab window is also uncertain (and is shown with a serrated edge), but since *Pesicek et al*. [2012] image a continuous slab at 35°S to 400 km, the slab window must terminate north of 35°S.

[60] In the context of structures that may influence the southern edge of the slab window, it is intriguing to note that extrapolation of the Mocha Fracture Zone (MFZ) coincides with the southern edge of our plume. However, *Tebbens and Cande* [1997] identify a putative piece of the MFZ 500 km west of South America. This western segment of a transform fault appears to end between chron 10 (∼28 Ma) and chron 13 (∼33 Ma), which implies that the matching segment of the transform fault on the other side of the spreading center must also end between chron 10 and chron 13. The age of the seafloor currently subducting where the

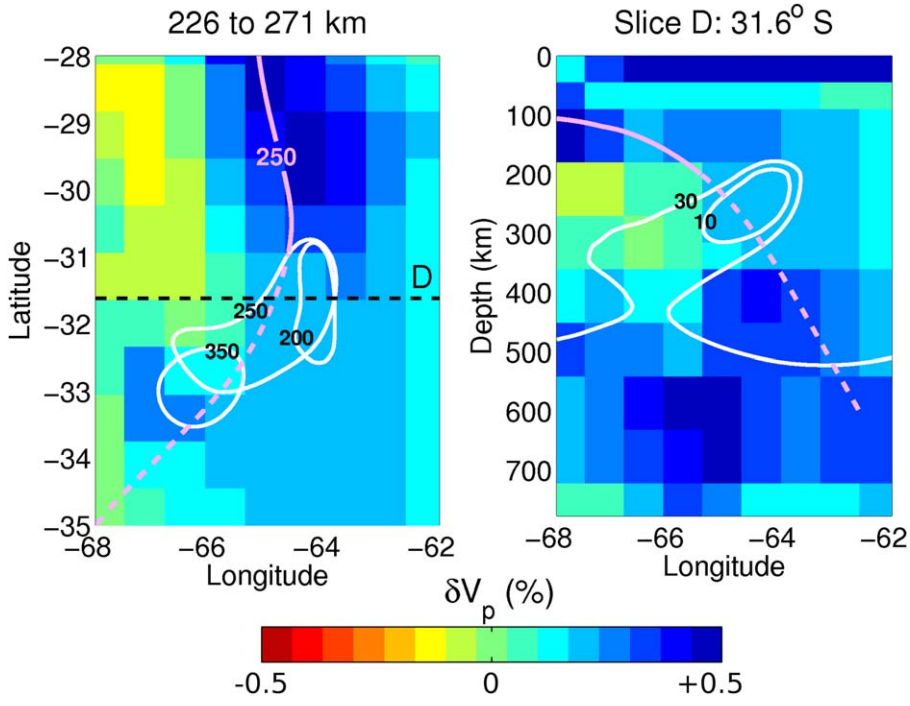

Figure 10. (left) horizontal slice of compressional seismic velocity perturbation (δV_p) centered at 249 km depth [*Li et al*., 2008]. The 250 km contour of the estimated top of the Nazca slab and the 10 Ohm m contours of the conductive plume at 200, 250 and 350 km depth are shown for comparison. The dashed line "D" is the location of slice *D* in Figure 5. (right) Vertical slice of the *Li et al*. [2008] model centered on slice *D*. The estimated top of the Nazca slab and the 10 and 30 Ohm m contours of the conductive plume at this slice are shown for comparison.

MFZ meets South America is between chron 10 and chron 13. Thus correlation of the two pieces of transform with the western and eastern ends of the MFZ is clearly reasonable and if correct, implies that the MFZ does not extend very far beneath South America. *Folguera and Ramos* [2009] in fact argue that subduction of the eastern end of the MFZ initiated deformation in the Andes at roughly 3.6 Ma and that the MFZ ends beneath the Andes at about (36.5°S, 71°W).

[61] The third alternative of electrically but not mechanically coupled plumes above and below the slab is not easy to dismiss. Above the top of the MTZ at 410 km, but deeper than 250 km it is extremely difficult to produce upper mantle resistivity of 10 Ohm m and less with high temperature and pressure alone [*Yoshino et al*., 2012]. Thus, low resistivity of the plume below the slab almost certainly requires either an interconnected fluid fraction with partial melt being the leading candidate [*Yoshino et al*., 2009] or a very high concentration of dissolved water (0.1%) [*Poe et al*., 2010]. If such a plume meets the slab it need not pass through to lower the slab resistivity. Instead it may locally elevate the slab temperature enough to release sufficient water to generate another plume rising above the slab. Such a slab "lesion" would have low seismic velocity and is very unlikely to be able to support tensile stress or generate seismicity and could thus explain the observations just as well as a plume that passes through a window in the slab. Since we cannot yet offer a definitive test of this alternative we have to leave it as an open possibility, but in the absence of other evidence pointing to this possibility, we conclude that a slab window is the most likely explanation for our results.

[62] Our electrically conductive plume is both similar to and different from the main conductive structure found by *Booker et al*. [2004] (see Figures 2 and 5b). Similarities include the fact that both structures are much more conductive than the surrounding mantle, and both structures appear to extend from near the top of the MTZ at 410 km depth but do not penetrate the base of the lithosphere at about 100 km. *Booker et al*. [2004], however, conclude that their conductor is parallel to and east of a steeply dipping slab. Our 3-D plume is very similar to *Booker et al*. [2004] down to 200 km but deviates more than 200 km to the

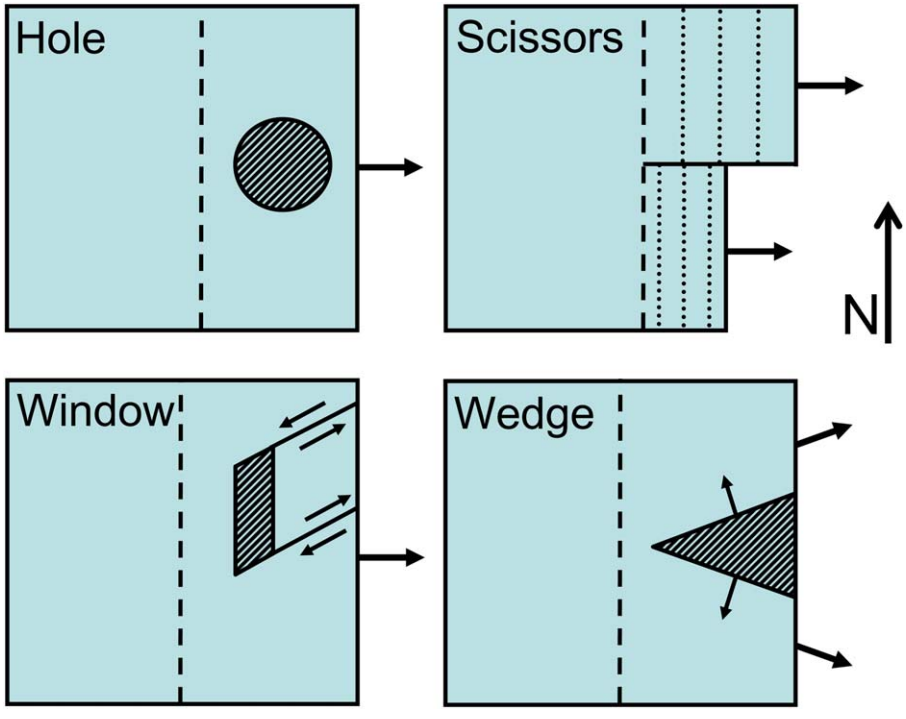

Figure 11. Four possible ways to create an opening in the slab through which the plume could pass: the "hole" caused by the plume itself; the "scissors"-style contour perpendicular tear as suggested by *Cahill and Isacks* [1992] with the south side dipping more steeply than the north side; the "window" opening initiated by contour-parallel normal faulting; and the "wedge"-style ripping, in which the slab is pulled laterally apart. Cross hatching indicates missing slab; dashed lines indicate the slab hinge; dotted lines indicated slab contours; large arrows indicate downdip direction; small arrows indicate slab motion or relative motion.

southwest as depth increases and thus cannot remain east of even a very steeply dipping slab. Nevertheless, the fundamental conclusion of *Booker et al*. [2004] from their 2-D study remains: there is a conductive feature extending up from near the 410 km seismic transition. It is encouraging that a 2-D interpretation of a clearly 3-D structure has such a close resemblance to the 3-D interpretation despite missing the necessity of the plume penetrating the slab.

[63] We can only speculate about why there is a slab window and an electrically conductive plume at this location. We consider four possibilities. (1) Since the plume conductivity is likely due to the presence of partial melt, it could be an asthenospheric plume such as has been suggested in the Cascadia back arc (G. Egbert, Three-dimensional Inversion of EarthScope Magnetotelluric Data: crustal and mantle conductivity beneath the NW USA, Incorporated Research Institutions for Seismology Webinar: http://www.iris.edu/hq/webinar/, 2013). (2) *Booker et al*. [2004] suggest that residual slab water at the intersection of the downgoing slab with the MTZ triggers the plume. This argument is no longer viable, as our plume and the projected Nazca slab enter the MTZ in different places. (3) Figure 10 suggests a relic slab in the MTZ under the origin of our plume: it is possible that the presence of this relic slab in the MTZ is responsible for the plume. (4) The plume is a consequence of the slab window's formation. We do not have an explanation for why this should be.

[64] The opening through which the plume passes may be caused by the plume itself or be the result of the geometry of the subduction. In addition to a plume-caused "hole," three variations are shown in Figure 11. The "scissors"-style contour-perpendicular tear configuration with vertical offset is suggested by *Cahill and Isacks* [1992]. This geometry requires the deep plume to jog to the southeast through the gap before rising further. It is clear from Figure 5c, however, that the plume jogs to the north-east, which would imply scissoring with the north side down and require the flat slab to be to the south. As this configuration does not exist, this type of tear can be ruled out. The "window" opening would start with contour-parallel normal faulting, with a piece of slab descending

faster. This is essentially a small version of a subducted oceanic ridge. Trench-parallel faults are known to exist in the slab [*Gans et al*., 2011], which at depth could allow denser, deeper slab to easily tear away. This kind of slab window requires strike-slip faulting. These strike-slip faults could be reactivated features parallel to the slab motion, such as those associated with the Juan Fernandez Ridge or perhaps the Mocha Fracture Zone. However, we favor "wedge"-style ripping in which the two pieces of slab are pulled laterally apart in an approximately north-south direction. The geometry of the flat slab produces significant lateral membrane stresses [*Creager et al*., 1995], which would be largely relieved upon opening of such a wedge. The plume should facilitate this process by heating the apex of the wedge. In this case, the wedge should probably extend downward through the entire slab, which would require that the deep slab shown on the right side of Figure 10 be a westward dipping relic slab, as discussed earlier. We propose that the termination of the very deep earthquakes at 29°S likely coincides with the northern boundary of the wedge.

5. Conclusion

[65] Results of a 3-D minimum-structure inversion yield an image of the electrical conductivity beneath the Pampean shallow subduction region in western Argentina. We have demonstrated the existence of an electrically conductive plume that passes through the extrapolated slab location at about 250 km. We conclude that a "wedge"-shaped slab window with its apex at the plume location best explains all the evidence.

Appendix A: Nazca Slab Contours Deeper Than 100 km From 23°S to 39°S

[66] To see whether the electrically conductive plume intersects the subducted slab it is neccessary to predict the slab depth below 200 km. We have constructed a slab that is consistent with available data and is extrapolated with minimum structure away from the constraints. Our goal was to produce a surface deeper than 150 km that is consistent with all available data. The result, valid from 100 to 600 km depth, is shown in Figure 12.

[67] This new slab surface is a minimum curvature fit to a series of constraints that are also presented in Figure 12. These constraints start with a subset of shallow contours that set the boundary condition on the shallow slab dip. From 33°S to 37°S we use the 140, 150, and 160 km contours of *Anderson et al*. [2007]. These contours are shown green on Figure 12a and are based on the Chile Argentina Geophysical Experiment (CHARGE) array [2000–2003] events plotted as small diamonds. North of 33°S we use the 100, 110, and 120 km contours of *Linkimer Abarca* [2011] shown light blue on Figure 12a. *Linkimer Abarca* [2011] uses the Sierras pampeanas Experiment using a Multicomponent Broad-band Array (SIEMBRA) (2007–2009) and Eastern Sierras Pampeanas (ESP) (2008–2010) array and has considerably more events (not shown) north of 31°S. These result in substantially different contours in the flattest portion of the slab, that are quite consistent with the EHB events [International Seismological Centre, EHB Bulletin, 2010] that are plotted.

[68] South of 37°S we use the 110, 150, and 170 km contours colored magenta on Figure 12a. They are contours of a plane fit to EHB events shown as a map in Figure 12b and in cross section in Figure 12c. The strike of this plane is determined to be 10.75°E of N at 39°S. The 110 km contour is seen to be almost exactly along the volcanic front, a coincidence which strengthens our result. Parallel planes +10 and −10 km from the best-fitting plane bound the scatter. However 18 events are not enough to decide whether this scatter represents the actual thickness of the seismogenic zone or statistical uncertainty. We simply use the best-fitting plane to estimate the slab surface because we are a long way from the flat slab region of primary interest and a 10 km error is of little consequence to our goal.

[69] To constrain the deeper parts of the slab, we transformed EHB hypocenters deeper than 500 km, 21.7° to 29°S and west of 62.5°W to Cartesian coordinates that correct for Earth's curvature. Figures 12d and12e show map and along-strike views of the plane that best fits the events with magnitude 4.0 or greater. Planes +10 and −10 km from and parallel to the best-fitting plane in Figure 12e define a tablet that again bounds the scatter. The number of events is much larger than in Figure 12c. The distribution appears relatively uniform across the thickness of this tablet and has abrupt edges. This argues that the spread of hypocenters is not simply statistical inaccuracy but may be due to a seismogenic zone about 20 km thick. Figure 12f shows the cross section when the magnitude cutoff is increased to 5.5. The strike direction has changed less than 0.5° and the dip by only slightly more than 1°. Otherwise the impression remains that the events are fairly uniformly distributed throughout the thickness of a 20 km thick tablet. We use the plane displaced +10 km as our best estimate of the slab top. The 500 and 600 km contours from 23°S and linearly extrapolated from 29°S to 30°S set the deep slab boundary condition. These contours are highlighted with magenta on Figure 12a.

[70] Finally, slab depths at approximately 10 km intervals along six transects labeled A, B, C, E, X24, and X35 on Figure 12a were added. The individual transects in cross sections with 1:1 vertical

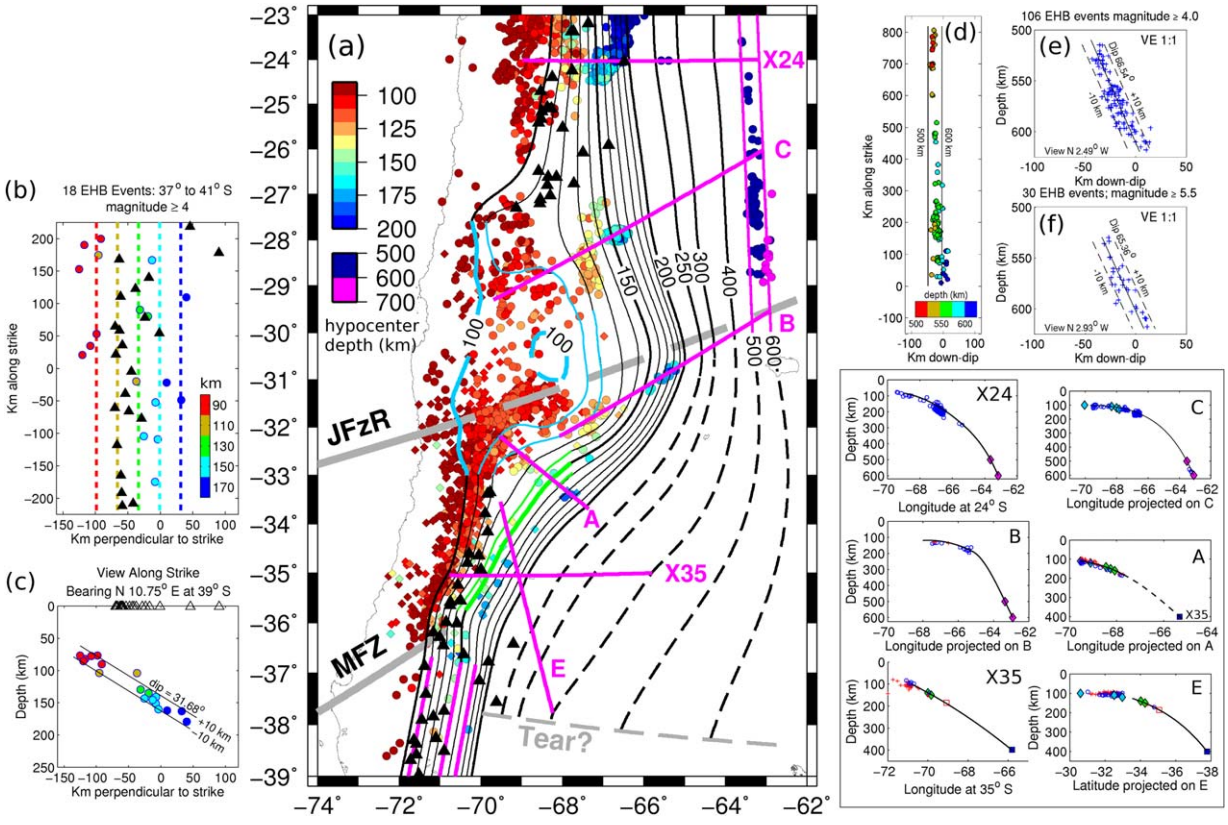

Figure 12. (a) Contours of the minimum curvature surface fit to a series of constraints on the Nazca slab surface deeper than 100 km. Contours are dashed where less certain. Circles filled with color indicating depth are earthquakes with magnitudes $\geq$ 4.0 from the EHB catalog (1960–2008). Diamonds are events from the CHARGE catalog (2000–2003). Black triangles are geologically recent volcanoes. JFzR = Juan Fernandez Ridge; MFZ = Mocha Fracture Zone. Contraints on the slab surface consist of: (1) light blue contours from *Linkimer Abarca* [2011]; (2) green contours from *Anderson et al*. [2007]; (3) magenta contours south of 37°S estimated by fitting a plane to EHB events as shown in (b) and (c); (4) magenta 500 and 600 km contours north of 30°S estimated by fitting a plane to deep EHB events from 21.7°S to 29°S as shown in (d)–(f); and (5) six magenta transects along which slab depth has been estimated at about 10 km spacing. Deep earthquakes with magnitude $\geq$ 4.0 color-coded with their depth are plotted in Figure 12d. The 500 and 600 km contours of the best-fitting plane are shown. Their cross section viewed along strike is shown in Figure 12e. The cross section (Figure 12f) repeats the fit using only events with magnitude > = 5.5. The data used to construct the transects A, B, C, E, X24, and X35 are summarized in 1:1 cross sections in the box. Crosses are CHARGE events within ±0.1° of the transect; circles are EHB events within the same windows; diamonds are intersections with constraint contours filled with contour color; open squares on transect B are Moment Tensor Centroids; the dark blue filled squares at 400 km on A, E, and X35 are estimated from the seismic tomographic slices of *Pesicek et al*. [2012]; the open squares on E and X35 are at the intersection of these two transects. The point labeled X35 on transect A is also on X35. The dashed portion of curve A is not used as a constraint. Finally, the termination of the Nazca slab in a "tear" at about 38°S is from *Pesicek et al*. [2012].

exaggeration are shown in the box together with the data used to determine the constraint curves. Unlike typically plotted transects, only hypocenters within ±0.1° (about 11 km) are projected onto each transect. This reduces bias associated with cross-transect slab geometry. Transects A, B, C, and X24 were chosen to maximize the number of events deeper than 150 km. Transects X35 and E coincide with seismic tomography model slices of *Pesicek et al*. [2012].

[71] Each constraint transect curve was constructed by fitting a second or third-order polynomial above 200 km to the top of the envelope of events from the CHARGE and EHB catalogs and the intersections with the *Anderson et al*. [2007] and *Linkimer Abarca* [2011] contours. Each curve is extrapolated below 200 km using a cubic spline that is constrained by the curve above 200 km and several different constraints at depth. North of 30°S, the estimated 500 and 600 km contours

set the slope of the deep slab. On X24, EHB events between 200 and 300 km are also used. On X35 and E, the position of the points at 400 km depth are estimated from the tomographic slices of *Pesicek et al*. [2012] which coincide with these transects. The 400 km deep point on E additionally coincides with downdip extrapolation of the plane shown in Figures 12b and 12c. Finally, the extrapolation of constraint A below 200 km agrees with the 400 km point on X35 although the dashed portion of curve A deeper than 200 km is not used as a constraint.

[72] A file with the slab surface in a format compatible with Generic Mapping Tools (GMT) is available as supporting information.[1]

Acknowledgments

[73] This project is supported by the U.S. National Science Foundation (NSF) grants EAR9909390, EAR0310113, and EAR0739116 and U.S. Department of Energy Office of Basic Energy Sciences grant DE-FG03–99ER14976. MT equipment is from the EMSOC Facility supported by NSF grants EAR9616421 and EAR0236538. This project also received support from the Agencia Nacional de Promoción Científica y Tecnológica PICT 2005 No. 38253. The first author received support from the Seattle Chapter of the ARCS Foundation, and from Graduate Research Support, Qamar, Stephens, and Coombs Fellowships provided by the Department of Earth and Space Sciences, University of Washington. Thank you to Jimmy Larsen for numerous helpful discussions, to Gabriel Giordanengo of Instituto de Geocronología y Geología Isotopíca for extensive assistance in the field, and to Paul Bedrosian for a constructive review. IRIS Data Management System, Seattle, Washington, the facilities of the IRIS Data Management System, and specifically the IRIS Data Management Center, were used for access to waveform, metadata or products required in this study. The IRIS DMS is funded through the National Science Foundation and specifically the GEO Directorate through the Instrumentation and Facilities Program of the National Science Foundation under Cooperative Agreement EAR-0552316. Some activities are supported by the National Science Foundation EarthScope Program under Cooperative Agreement EAR-0733069.

References

Anderson, M., P. Alvarado, G. Zandt, and S. Beck (2007), Geometry and brittle deformation of the subducting Nazca Plate, Central Chile and Argentina, *Geophys. J. Int.*, *171*, 419–434, doi:10.1111/j.1365-246X.2007.03483.x.

Bahr, K. (1988), Interpretation of the magnetotelluric impedance tensor regional induction and local telluric distortion, *J. Geophys.*, *62*(2), 119–127.

Booker, J. R. (2013), The magnetotelluric phase tensor: A critical review, *Surv. Geophys.*, doi:10.1007/s10712-013-9234-2.

Booker, J. R., A. Favetto, and M. C. Pomposiello (2004), Low electrical resistivity associated with plunging of the Nazca flat slab beneath Argentina, *Nature*, *429*, 399–403, doi:10.1038/nature02565.

Booker, J. R., A. Favetto, M. C. Pomposiello, and F. Xuan (2005), The role of fluids in the Nazca flat slab near 31s revealed by the electrical resistivity structure, in 6th International Symposium on Andean Geodynamics, Barcelona, Spain, pp. 119–122, IRD Editions Montpellier.

Cahill, T., and B. Isacks (1992), Seismicity and shape of the subducted Nazca plate, *J. Geophys. Res.*, *97*, 17,503–17,529, doi:10.1029/92JB00493.

Caldwell, G. C., H. M. Bibby, and C. Brown (2004), The magnetotelluric phase tensor, *Geophys. J. Int.*, *158*, 457–469, doi:10.1111/j.1365-246X.2004.02281.x.

Chen, P.-F., C. R. Bina, and E. A. Okal (2001), Variations in slab dip along the subducting Nazca Plate, as related to stress patterns and moment release of intermediate-depth seismicity and to surface volcanism, Geochem. *Geophys. Geosyst.*, *2*(12), 1054, doi:10.1029/2001GC000153.

Creager, K. C., L. Chiao, J. P. Winchester, and E. R. Engdahl (1995), Membrane strain rates in the subducting plate beneath South America, *Geophys. Res. Lett.*, *22*, 2321–2324, doi:10.1029/95GL02321.

Egbert, G. (1997), Robust multiple-station magnetotelluric data processing, *Geophys. J. Int.*, *130*, 475–496, doi:10.1111/j.1365-246X.1997.tb05663.x.

Folguera, A., and V. Ramos (2009), Collision of the Mocha fracture zone and a <4 Ma old wave of orogenic uplift in the Andes (36°–38°S), *Lithosphere*, *1*, 364–369, doi:10.1130/L66.1.

Gans, C. R., S. L. Beck, G. Zandt, H. Gilbert, P. Alvarado, M. Anderson, and L. Linkimer (2011), Continental and oceanic crustal structure of the Pampean flat slab region, western Argentina, using receiver function analysis: New high-resolution results, *Geophys. J. Int.*, *186*, 45–58, doi:10.1111/j.1365-246X.2011.05023.x.

Groom, R. W., and R. C. Bailey (1989), Decomposition of magnetotelluric impedance tensors in the presence of local three dimensional galvanic distortion, *J. Geophys. Res.*, *94*, 1913–1925, doi:10.1029/JB094iB02p01913.

International Seismological Centre (2010), *EHB Bull.*, Int. Seismol. Cent., Thatcham, U. K. [Available at http://www.isc.ac.uk.].

Jones, A. G. (2012), Distortion of magnetotelluric data: Its identification and removal, in *The Magnetotelluric Method Theory and Practice*, edited by A. Chave and A. Jones, Cambridge Univ. Press, Cambridge.

Li, C., R. D. van der Hilst, E. R. Engdahl, and S. Burdick (2008), A new global model for P wave speed variations in Earth's mantle, *Geochem. Geophys. Geosyst.*, *9*, Q05018, doi:10.1029/2007GC001806.

Linkimer Abarca, L. (2011), Lithospheric structure of the Pampean flat slab (Latitude 30–33S) and Northern Costa Rica (Latitude 9–11N) subduction zones, PhD thesis, Univ. of Ariz., Tucson.

Mackie, R. L., W. Rodi, and M. D. Watts (2001), 3-D magnetotelluric inversion for resource exploration, in SEG 2001 Technical Program Expanded, Soc. of Explor. Geophys., San Antonio, Tex.

Pardo, M., D. Comte, and T. Monfret (2002), Seismotectonic and stress distribution in the central Chile subduction zone, *J. South Am. Earth Sci.*, *15*, 11–22, doi:10.1016/S0895–9811(02)00003-2.

[1]Additional supporting information may be found in the online version of this article.

Pesicek, J. D., E. R. Engdahl, C. H. Thurber, H. R. DeShon, and D. Lange (2012), Mantle subducting slab structure in the region of the 2010 M8.8 Maule earthquake (30–40° S), Chile, *Geophys. J. Int.*, *191*, 317–324, doi:10.1111/j.1365-246X.2012.05624.x.

Petiau, G. (2000), Second generation of Lead-lead chloride electrodes for geophysical applications, *Pure Appl. Geophys.*, *157*(3), 357–382, doi:10.1007/s000240050004.

Poe, B. T., C. Romano, F. Nestola, and J. R. Smyth (2010), Electrical conductivity anisotropy of dry and hydrous olivine at 8 GPa, *Phys. Earth Planet. Inter.*, *181*, 103–111, doi:10.1016/j.pepi.2010.05.003.

Ramos, V. A. (2009), Anatomy and global context of the Andes: Main geologic features and the Andean orogenic cycle, in *Backbone of the Americas: Shallow Subduction, Plateau Uplift, and Ridge and Terrane Collision*, vol. 204, edited by S. Kay, V. Ramos, and W. Dickinson, pp. 31–65, Geol. Soc. of Am., doi:10.1130/2009.1204(02), Boulder.

Rodi, W., and R. L. Mackie (2001), Nonlinear conjugate gradients algorithm for 2-D magnetotelluric inversion, *Geophysics*, *66*, 174–187, doi:10.1190/1.1444893.

Slancová, A., A. Špičák, V. Hanuš, and J. Vaněk (2000), Delimitation of domains with uniform stress in the subducted Nazca plate, *Tectonophysics*, *319*, 339–364, doi:10.1016/S0040–1951(99)00302-9.

Smith, J. T., and J. R. Booker (1991), Rapid inversion of two- and three-dimensional magnetotelluric data, *J. Geophys. Res.*, *96*, 3905–3922, doi:10.1029/90JB02416.

Tebbens, S. F., and S. C. Cande (1997), Southeast Pacific tectonic evolution from early Oligocene to present, *J. Geophys. Res.*, *102*, 12,061–12,084, doi:10.1029/96JB02582.

Xu, Y., T. Brent, T. Poe, T. Shankland, and D. Rubie (1998), Electrical conductivity of olivine, wadsleyite and ringwoodite under upper-mantle conditions, *Science*, *280*, 1415–1418, doi:10.1126/science.280.5368.1415.

Xu, Y., T. Shankland, and T. Poe (2000), Laboratory-based electrical conductivity in the earth's mantle, *J. Geophys. Res.*, *105*, 27,865–27,875, doi:10.1029/2000JB900299.

Yoshino, T. (2010), Laboratory electrical conductivity measurement of mantle minerals, *Surv. Geophys.*, *31*, 163–206, doi:10.1007/s10712-009-9084-0.

Yoshino, T., T. Matsuzaki, A. Shatskiy, and T. Katsura (2009), The effect of water on the electrical conductivity of olivine aggregates and its implications for the electrical structure of the upper mantle, *Earth Planet. Sci. Lett.*, *2008*, 291–300, doi:10.1016/j.epsl.2009.09.032.

Yoshino, T., A. Shimojuku, S. Shan, X. Guo, D. Yamazaki, E. Ito, Y. Higo, and K. Funakoshi (2012), Effect of temperature, pressure and iron content on the electrical conductivity of olivine and its high-pressure polymorphs, *J. Geophys. Res.*, *117*, B08205, doi:10.1029/2011JB008774.